STELLAR ASTROPHYSICS WITH A DISPERSED FOURIER TRANSFORM SPECTROGRAPH. I. INSTRUMENT DESCRIPTION AND ORBITS OF SINGLE-LINED SPECTROSCOPIC BINARIES

Bradford B. Behr[1,2], Arsen R. Hajian[1], Andrew T. Cenko[1], Marc Murison[3], Robert S. McMillan[4], Robert Hindsley[5], and Jeff Meade[1]

[1] Department of Systems Design Engineering, University of Waterloo, Waterloo ON N2L 3G1, Canada
[2] Eureka Scientific, 2452 Delmer Street Suite 100, Oakland, CA 94602-3017, USA
[3] US Naval Observatory, Flagstaff Station, 10391 W. Naval Observatory Rd., Flagstaff, AZ 86001, USA
[4] Lunar and Planetary Laboratory, University of Arizona, Tucson, AZ 85721, USA
[5] Remote Sensing Division, Naval Research Laboratory, Code 7215, Washington, DC 20375, USA

ABSTRACT

We have designed and constructed a second-generation version of the dispersed Fourier transform spectrograph, or dFTS. This instrument combines a spectral interferometer with a dispersive spectrograph to provide high-accuracy, high-resolution optical spectra of stellar targets. The new version, dFTS2, is based upon the design of our prototype, with several modifications to improve the system throughput and performance. We deployed dFTS2 to the Steward Observatory 2.3 m Bok Telescope from 2007 June to 2008 June, and undertook an observing program on spectroscopic binary stars, with the goal of constraining the velocity amplitude K of the binary orbits with 0.1% accuracy, a significant improvement over most of the orbits reported in the literature. We present results for radial velocity reference stars and orbit solutions for single-lined spectroscopic binaries.

Key words: binaries: spectroscopic – instrumentation: spectrographs – techniques: radial velocities

1. INTRODUCTION

For high-resolution ($R = \lambda/\Delta\lambda \simeq 50,000$) spectroscopy of stellar targets, most astronomers use cross-dispersed echelle spectrographs. When equipped with an iodine absorption cell or a thorium–argon calibration source, echelle spectrographs can measure the radial velocity (RV) of a star with a precision of $\sim$1 m s^{-1} (Bouchy et al. 2009; Howard et al. 2009). This approach to stellar velocimetry has proven highly successful in the hunt for exoplanets and other low-mass, low-luminosity companions orbiting bright stars.

However, the application of these "precision radial velocity" (PRV) techniques to binary stars has been more limited. Models of stellar structure and evolution require accurate measurement of stellar masses for validation and refinement, and binary star systems are among the best celestial laboratories for making such measurements. Given the period P, RV amplitudes K_1 and K_2 of the two components, eccentricity e, and inclination angle i of a double-lined spectroscopic binary (SB2) system, the masses of both stars can easily be derived. If the angular size of the semimajor axes of the orbit can also be measured, using spatial or speckle interferometry, then the distance to the system can be determined as well.

When an SB2 target is observed with an iodine-absorption echelle, it becomes algorithmically challenging to disentangle the three superposed spectra (two different stars plus the iodine absorption lines). Konacki (2005, 2009) has made notable progress toward solving this challenge, and in conjunction with astrometric data from spatial interferometers, his technique has yielded some very precise binary star masses (Muterspaugh et al. 2006), but this approach has not yet been widely adopted.

Thorium–argon emission line lamps provide another means of precisely determining the wavelength scale for echelle spectra, and several groups have achieved excellent RV results on spectroscopic binaries using Th–Ar calibration. Tomkin & Fekel (2006) reported rms velocity residuals of 0.11 km s^{-1} on two SB2 systems, a particularly notable accomplishment given

that their spectrograph, the Sandiford Echelle (McCarthy et al. 1993), is mounted at the Cassegrain focus of the telescope, and is thus subject to a changing gravity vector. Fekel et al. (2007) achieved a similar level of RV precision with a fiber-fed, bench-mounted echelle. The HERCULES instrument (Hearnshaw et al. 2002), a fiber-fed echelle mounted inside a vacuum chamber for greater RV stability, has achieved impressive rms velocity residuals of 14–56 m s^{-1} on binary targets (Ramm et al. 2004; Skuljan et al. 2004; Ramm 2008).

Our research group has been pursuing an alternative approach to stellar velocimetry, developing a new instrument which provides meter-per-second RV accuracy without a superposed reference spectrum or vacuum enclosure. This instrument concept is known as the dispersed Fourier transform spectrograph, or dFTS. Our prototype device, dFTS1, is described in detail by Hajian et al. (2007, henceforth, "Paper 1"). Installed at the Clay Center Observatory 0.6 m telescope, dFTS1 demonstrated the viability of the concept, with precision RV measurements of spectroscopic binary systems and exoplanet host stars.
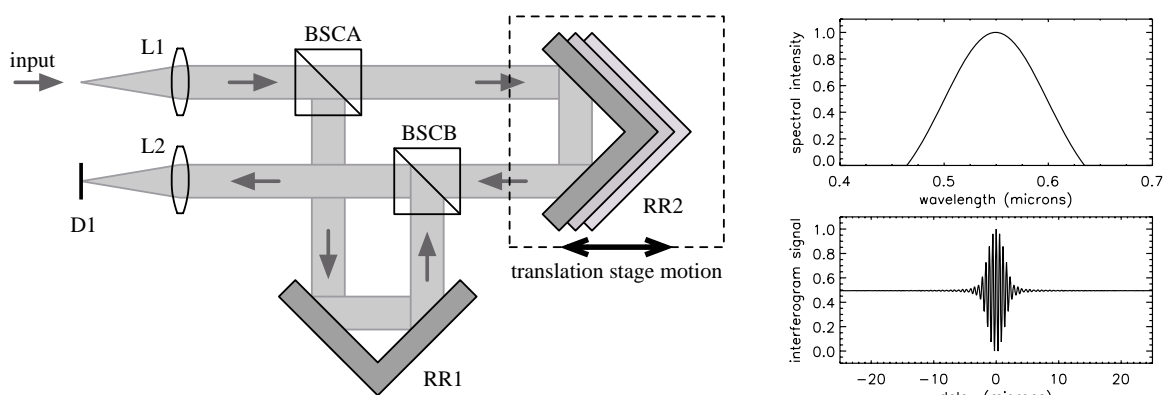
To develop the dFTS concept further and undertake a comprehensive science program, we designed and constructed a new device, called dFTS2, and deployed it at the Steward Observatory 2.3 m Bok Telescope on Kitt Peak. In this paper, we describe the dFTS2 instrument and present results from our observing campaign, focusing on RV reference stars and single-lined spectroscopic binary stars (SB1s). Single-lined binaries are not as scientifically interesting as SB2s, because absolute stellar masses cannot be derived, but the SB1s still serve as useful tests of our spectrograph performance. Orbital elements of double-lined systems will be discussed in a subsequent paper.

## 2. OVERVIEW OF THE dFTS CONCEPT

The dFTS concept and its underlying mathematical theory are treated in detail in Paper 1, but in the following section we review some of the key aspects of the design.

A traditional Fourier transform spectrograph (FTS) consists of a Michelson interferometer with one retroreflector mounted

Report Documentation Page

1. REPORT DATE **01 NOV 2009**	2. REPORT TYPE	3. DATES COVERED **00-00-2009 to 00-00-2009**
4. TITLE AND SUBTITLE **Stellar Astrophysics With a Disperesed Fourier Transform Spectrograph. 1. Instrument Description and Orbits of Single-Lined Spectrosopic Binaries**		5a. CONTRACT NUMBER
		5b. GRANT NUMBER
		5c. PROGRAM ELEMENT NUMBER
6. AUTHOR(S)		5d. PROJECT NUMBER
		5e. TASK NUMBER
		5f. WORK UNIT NUMBER
7. PERFORMING ORGANIZATION NAME(S) AND ADDRESS(ES) **Department of Systems Design Engineering,University of Waterloo,Waterloo ON N2L 3G1, Canada, ,**		8. PERFORMING ORGANIZATION REPORT NUMBER
9. SPONSORING/MONITORING AGENCY NAME(S) AND ADDRESS(ES)		10. SPONSOR/MONITOR'S ACRONYM(S)
		11. SPONSOR/MONITOR'S REPORT NUMBER(S)
12. DISTRIBUTION/AVAILABILITY STATEMENT **Approved for public release; distribution unlimited**		
13. SUPPLEMENTARY NOTES		
14. ABSTRACT		
15. SUBJECT TERMS		

16. SECURITY CLASSIFICATION OF:			17. LIMITATION OF ABSTRACT **Same as Report (SAR)**	18. NUMBER OF PAGES **11**	19a. NAME OF RESPONSIBLE PERSON
a. REPORT **unclassified**	b. ABSTRACT **unclassified**	c. THIS PAGE **unclassified**			

Figure 1. Schematic of a conventional FTS using an offset Michelson interferometer configuration (left), with a broadband input spectrum (top right) and resulting interferogram (bottom right).
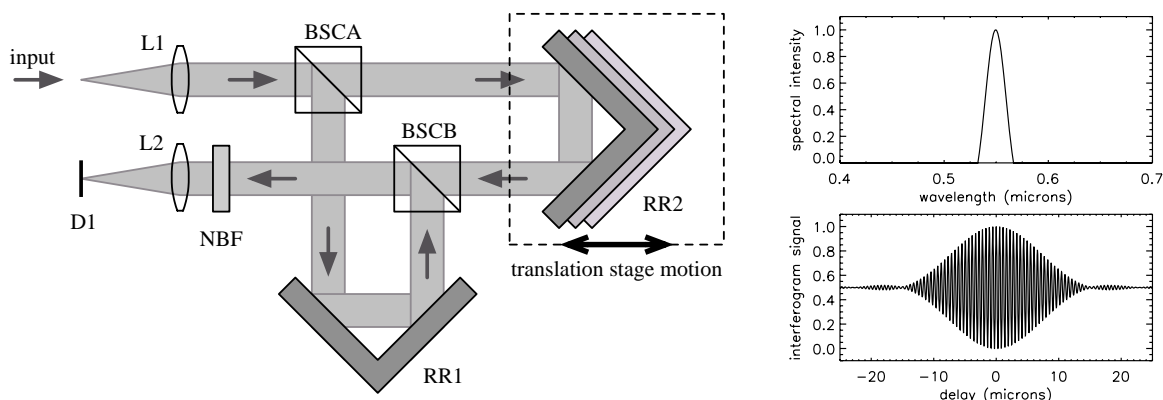
Figure 2. Schematic of a conventional FTS with a narrowband filter (left). The narrowed spectral bandpass (top right) results in a broader central fringe packet in the interferogram (bottom right), such that the fringes at large delay are stronger than in Figure 1.

on a translation stage (Figure 1, left). An input source is collimated and then divided into two equal parts by a beam-splitter cube (BSCA). Each beam travels down one "arm" of the interferometer, hits a corner-cube retroreflector (RR1 or RR2), and returns to a second beam splitter (BSCB), where the two beams combine interferometrically. Depending on the wavelength of the light and the optical path difference (OPD) or "delay" between the two arms, the outputs from BSCB will exhibit constructive or destructive interference (in the figure, only one output is shown; a complementary output exits the top face of BSCB.).

As RR2 is moved on its translation stage, the delay changes, and the intensity of the interferometer output changes as well. Normally, the retroreflector stage is scanned or stepped through a series of different positions, and the output intensity at each delay is measured using a photosensitive detector (D1). The result is an interferogram (Figure 1, bottom right), which is the Fourier transform of the spectral energy distribution of the input source (Figure 1, top right). By performing a Fourier inversion of the interferogram, the source spectrum can be recovered. For a higher-resolution spectrum, the interferometer merely needs to scan over a wider range of delay, and the wavelength scale of the spectrum can be derived very accurately if the delay positions are measured with a metrology system.

However, if the input source is broadband, as depicted in Figure 1, then the amplitude of a FTS's interferometric "fringes" (the oscillations of intensity as a function of delay) drops off quickly as we move away from the central delay position (OPD = 0), because all the different wavelengths quickly

decorrelate. Small-amplitude fringes are still present, but they become very difficult to detect given measurement noise. Fine details of the input spectrum, which are encoded in the high-delay fringes, are thus lost.

To boost the fringe contrast, a narrowband filter (NBF) can be added to a FTS, thereby restricting the input bandpass (Figure 2). The interferometer output remains coherent over a wider range of delays, with stronger fringes at large delay, so that details of the spectrum can be measured. However, all light outside the filter bandpass is discarded. For some astronomical applications, where only a narrow spectral region is of interest, this is acceptable, but for broadband spectroscopy, the overall system efficiency is unacceptably low. Traditional FTS devices have therefore seen only limited use in stellar astronomy.

The dFTS concept addresses this limitation of the traditional FTS design. Figure 3 depicts a dFTS configuration in a schematic form. The narrowband filter has been replaced by a dispersive grating (G), and the dispersed spectrum is focused onto an array detector (CCD). The broadband output beam from the interferometer is thus divided into many separate spectral channels (Figure 3, top right), each of them covering just a small subsection of the initial bandpass. The figure shows only six channels, but in an actual dFTS instrument, there would be thousands of channels, one for each CCD pixel along the dispersion dimension. Because the channels are narrowband, their fringe patterns (Figure 3, bottom right) span a wide range of delays, and we can derive the fine details of the spectrum from the high-OPD fringes without sacrificing spectral coverage. In essence, the grating acts as a multiplexer, converting a
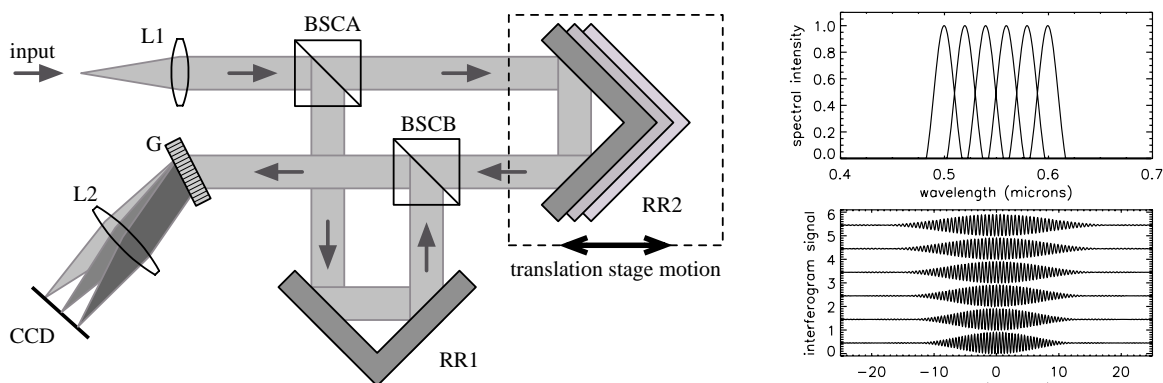
Figure 3. Schematic of a dispersed FTS (left). The Michelson interferometer is followed by a grating spectrograph, which acts as a multiplexer. Each pixel along the CCD's dispersion axis acts as the detector for a separate spectral channel (top right). Because the individual channels are narrowband, their interferograms (bottom right) have wide central fringe packets and stronger fringes at large delay than in the broadband case.

single broadband FTS into several thousand narrowband FTSs, all operating in parallel and sharing the same interferometer optics. Each channel interferogram transforms into a narrowband spectrum. Merging the narrowband spectra produces a high-resolution broadband spectrum.

An additional advantage of narrowband output channels is that the interferogram can be sampled much more coarsely. The Nyquist theorem requires that, in order to avoid aliasing, the fringes must be sampled with a delay step size Δx which is less than or equal to $1/(2\Delta s)$, where Δs is the bandwidth in wavenumbers. With narrowband channels, therefore, we can cover a wide range of delays (and thus derive a high-resolution spectrum) with relatively few delay positions. This "sparse-sampling" strategy is treated in more detail in the Appendices of Paper 1.

Two additional strengths of the dFTS concept should be noted. First, the instrumental broadening function (or line spread function) can be determined a priori from the delay sampling function, so that the true shape of the stellar absorption line profiles can be derived in a straightforward fashion. Second, because the high-resolution information in the source spectrum is extracted by the interferometer, the dispersive part of the dFTS does not have to be as powerful as in an echelle (e.g., $R = 5000$ instead of $R = 50,000$), so the collimated beam diameter at the disperser can be considerably smaller. This issue is particularly relevant for instruments on 8–10 m telescopes, where the instrument optics can become exceedingly large and expensive. Smaller-diameter optics are also advantageous for instruments in spacecraft, airborne platforms, and field-portable sensor packages.

3. INSTRUMENT DESIGN AND DEPLOYMENT

3.1. Design Considerations

The dFTS1 prototype proved successful for validating the instrument concept and demonstrating its capabilities for accurate measurement of stellar RVs, but in the course of commissioning and operating dFTS1 we identified several potential improvements to the optical design and implementation. The design of dFTS2 was thus motivated by five main drivers:

1. Higher photon throughput.
2. Higher spectral resolution R_G of the dispersive back end, for narrower channel bandpasses and higher fringe contrast over the delay range.
3. Good coupling to 2 m telescope optics.

4. Smaller physical size, for transportation to observing facilities.
5. Utilization of optics and optomechanical components that were already in hand, or could be acquired inexpensively, to fit within our budget constraints.

3.2. Final Instrument Design

The final configuration of dFTS2 is shown in Figure 4. The interior of the instrument's thermal enclosure measures approximately 100 cm × 70 cm, with a height of 30 cm. The interferometer and the laser metrology system are mounted on a larger optical breadboard (on the left side of the photograph in Figure 4), while the dispersive back end is placed on a smaller separate breadboard (on the right side), so that vibrations from the mechanical shutter and CCD fans would not affect the interferometer.

Starlight from the telescope enters the instrument via a multimode fiber (MMF). The beam exiting the fiber is collimated by a lens L1 and passes through an iris with 20 mm aperture. It then encounters BSC1, the first of four polarizing beam-splitter cubes. BSC1 is mounted at a 45° angle from the plane of the breadboard, so the transmitted light is diagonally (linearly) polarized. At BSC2 (which corresponds to BSCA in the prior figures), the vertically polarized component of the beam is reflected toward the stationary retroreflector, RR1, while the horizontally polarized part transmits and goes to the moving retroreflector, RR2. For translating RR2, we use an Aerotech ANT-50L linear motor stage, instead of the Parker Daedal MX-80 stage in dFTS1 (as described in Paper 1). The ANT-50L provides better stability while holding at a fixed delay position; the rms jitter in optical delay position is typically less than 20 nm.

After retroreflection, the beams meet at BSC3 (equivalent to BSCB), where the vertically polarized beam is again reflected and the horizontally polarized beam is transmitted, such that the beams are once more coincident and parallel. Because of their orthogonal polarizations, however, they cannot combine interferometrically until they encounter BSC4, which is mounted at 45° like BSC1 and thus "mixes" the two polarizations together. The two outputs from BSC4 (one transmitted, one reflected) are each focused by a lens L2, are steered by a series of fold mirrors (FM), and are passed through the shutter S en route to the dispersive back end of the instrument. The light that is reflected from BSC1 (the "C-beam") is focused by a third L2 lens, and also enters the back end, where it provides a non-interferometric flux reference.
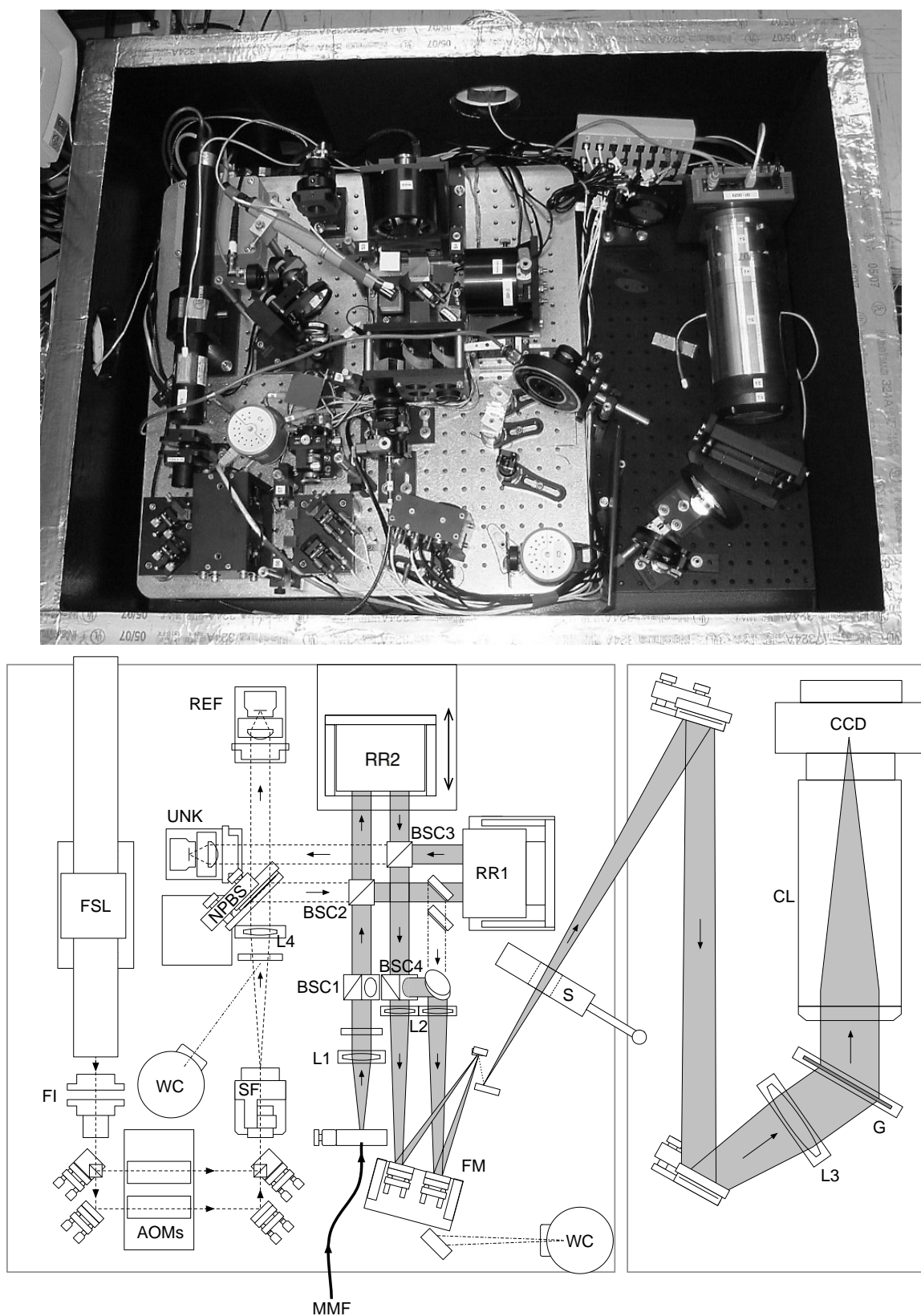
Figure 4. Photograph and layout schematic of the final dFTS2 design. Gray sections show the starlight beams, dashed lines delineate the laser metrology beams, and dot-dash lines indicate beam paths for optical alignment; see the text for explanation of the component codes.

We had originally placed a set of optical fiber spot-to-line bundles just prior to the shutter, in order to "slice" the output beams from the interferometer, and thus achieve higher grating resolution R_G in the dispersive back end. We used this fiber arrangement for the first observing run but found that it was very inefficient, so we replaced it with an arrangement of small mirrors before the second observing run.

The three diverging beams are collimated by achromat L3 and then dispersed by grating G, a Kaiser Optical Systems Inc. volume–phase holographic grating with 1800 lines mm^{-1}. For the camera lens (CL), one of us (Murison) designed a custom $f/3.6$ lens with 180 mm focal length, using only off-the-shelf singlets and achromats. When installed prior to the second observing run, this custom lens provided a vast improvement in photon efficiency over the Nikon SLR lens that we had been using previously. The lens is bolted to an Apogee U-1107 CCD, with a 2048×122 array of 12 μm $\times$ 12 μm pixels. The total instrument bandpass spans from 470 nm to 540 nm.

As with dFTS1, a laser metrology system continuously monitors the optical delay during a data acquisition scan, so that each delay position is precisely and unambiguously known. A Melles–Griot 05-STP-901 frequency-stabilized laser (FSL) acts as the wavelength reference. The laser beam passes through a Faraday isolator (to suppress backscatter) and is then divided into horizontally and vertically polarized components by a small polarizing BSC. These beams are frequency-shifted by two acousto-optic modulators (AOMs), which are driven at two slightly different frequencies, creating an 11 kHz beat frequency between the horizontal and vertical polarizations. The two polarizations are recombined by a second small BSC, and then sent through a spatial filter (SF) to produce a flat and uniform wavefront. Lens L4 collimates the metrology beam to a diameter of 20 mm, matching the starlight beam size. A non-polarizing 50/50 beam splitter (NPBS) sends half of the metrology beam into the interferometer, while the other half goes to a "reference" metrology detector (REF), where the horizontal and vertical components of the beam are mixed together with a linear polarizer, and the resulting 11 kHz sinusoidal interference signal is detected by a photodiode. The metrology beam enters the interferometer at BSC2, following exactly the same path as the starlight beam until BSC3, where it exits and is captured by the "unknown" metrology detector unit (UNK), which also detects the 11 kHz sinusoidal signal. A change in the interferometer delay manifests as a phase shift between the REF and UNK signals. This phase difference is measured and recorded, and then converted into an absolute delay position in post-processing.

The dFTS2 instrument is housed inside a thermal enclosure, with a temperature stabilization system that keeps the internal air temperature constant to ± 0.05 °C. A Vaisala PTU-200 atmospheric monitoring unit measures the temperature, pressure, and humidity of the airmass in the immediate vicinity of the interferometer, so that we can correct our laser metrology data to account for changes in the index of refraction, which would otherwise induce shifts of $\sim$20 m s^{-1} in the RV zero point of the instrument. Key optical components are placed on tip-tilt mounts with New Focus "Picomotor" actuators, for remote adjustment, and critical beam alignment positions are viewed remotely with D-Link DCS-900 webcams (WC).

3.3. Telescope Guider Box and Fiber Feed

Starlight reaches the dFTS2 instrument via a multimode optical fiber from a customized "guider box" that bolts to the telescope's Cassegrain focus position. The $f/9$ converging beam from the telescope's secondary mirror reflects from a SBIG AO-7 tip-tilt mirror and then passes through a small achromat lens, which speeds up the beam to $f/2.5$. Just before encountering the input tip of the fiber, the beam passes through an uncoated pellicle (92% transmission). The 50 μm core of the fiber subtends 1″.8 on the sky. The light that does not enter the fiber is reflected by the polished face of the fiber ferrule, and 8% of it bounces off the pellicle and is reimaged on to an Astrovid StellaCam III video camera, which provides an image for guiding. This video signal is digitized and monitored by a custom software package, which adjusts the AO-7 tip-tilt mirror to keep the star image centered on the fiber core.

Light from calibration sources (such as an incandescent lamp or a hollow-cathode emission-line lamp) is sent to the guider box through a secondary optical fiber. The output from this fiber is reimaged onto the primary fiber input via a fold mirror which is inserted into the telescope beam path, so that the calibration source reaches the main fiber from the same direction and at the same f/ratio as starlight. This feature of dFTS2 ensures that the instrument illumination pattern is the same for calibration and science exposures.

3.4. Deployment and Operation

The dFTS2 hardware was assembled at the US Naval Observatory in Washington, D.C., and after a brief testing period was shipped to Steward Observatory's 2.3 m Bok Telescope on Kitt Peak in Arizona. For the initial commissioning run, we installed the instrument and support electronics in a storage room one floor below the telescope, but this room was not air-conditioned, and the instrument was prone to overheating, so for subsequent runs we moved dFTS2 to the control room next to the telescope. The thermal environment was more stable at this location, although the temperature stabilization system still had to contend with fluctuations of $\sim$ 4 °C in the ambient air temperature as the room's A/C or heating system cycled.

We had eight observing runs on the Bok Telescope with dFTS2, on the following dates (civil): 2007 June 27–July 4; 2007 September 30–October 3; 2007 October 27–31; 2008 January 22–27; 2008 March 22–24; 2008 April 20–23; 2008 May 16–20; and 2008 June 17–21.

Interferometric scans on stellar targets consisted of 500 delay step positions, with a 0.25–4.0 s exposure at each position, depending on the star's brightness and the atmospheric seeing and opacity.

4. INSTRUMENT PERFORMANCE

4.1. Photon Throughput

To test the real-world photon efficiency of the instrument, we measured the photoelectron detection rate on our CCD while observing photometrically stable stars under good seeing conditions, and compared those numbers to the expected photon flux as determined from the stars' published V magnitudes. We estimate the total system efficiency (including atmospheric opacity, telescope mirror reflectivity, fiber feed transmission, instrument mirror reflectivity, and CCD quantum efficiency) to be 4.3%. This figure represents a significant ($6\times$) improvement over the 0.7% total efficiency we reported for dFTS1. The enhanced throughput performance of dFTS2 is due primarily to better coupling into the fiber in the telescope guider box, a simpler instrument layout with fewer fold mirror reflections, and the custom camera lens. In conjunction with the larger collecting area of the Bok Telescope, these upgrades have permitted us to achieve much better RV precision on fainter stars than with dFTS1.

However, further improvements in photon throughput are certainly possible. The 50 μm core diameter of the optical fiber was not well matched to the typical seeing disk size at the Bok Telescope; with a 100 μm fiber and suitable
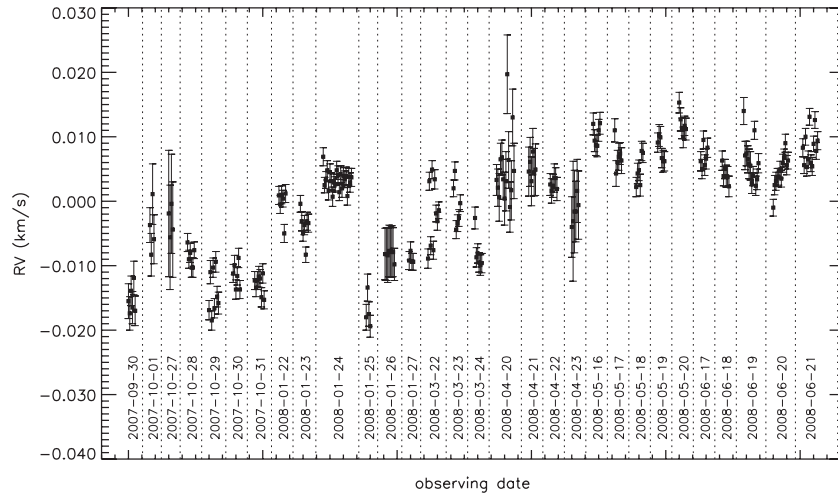
Figure 5. Night-to-night RV zero point of dFTS2, measured using a thorium–neon emission-line lamp.

modifications to the downstream optics, we might have achieved a 50%–80% increase in the measured stellar flux. The optics in the dFTS2 instrument box also accumulated some visible dust over the course of our observing campaign, despite our efforts to keep the system enclosed as much as possible during assembly and disassembly. With future dFTSes permanently installed as facility instruments, we anticipate being able to reach photon throughput efficiencies of 10%–12%, similar to many echelle spectrographs.

4.2. Dispersive Back-end Resolution

During each night of observing, we collected an interferometric scan of a incandescent white-light source, which let us measure the central wavelength and the bandwidth of each spectral channel on the CCD. These channel bandpass data are subsequently used in reconstructing the broadband high-resolution spectra of our stellar targets and measuring their RVs. We can also use these white-light scans to evaluate the performance of the dispersive back-end system. We measure a spectral resolution of $R_G > 4700$ over the entire spectral range of dFTS2, with a mean R_G of approximately 4950 and a peak of 5150. This resolution is nearly three times better than the $R_G \simeq 1700$ of dFTS1, which results in broader fringe packets, greater fringe visibility, and thus better signal-to-noise ratio of the final high-resolution spectra.

4.3. Intrinsic RV Stability

In addition to the white-light scans, we also acquired at least six scans of a hollow-cathode thorium–neon emission-line lamp per night. (The only available thorium–argon lamp was not bright enough for reliable measurements.) By measuring the interferometric fringe patterns of the ~60 brightest emission lines, we were able to evaluate the intrinsic RV stability of the instrument. These calibration measurements also defined the RV zero point for each night of an observing run; when the instrument was reassembled at the beginning of each run, or realigned during a run, the alignment between the starlight and metrology beams could have shifted slightly, creating a systematic offset in derived RV.

Figure 5 shows the measured RVs of the thorium–neon source for 224 scans over the course of our observing program, from 2007 September to 2008 June. On some nights, such as 2008 January 24 and 2008 April 22, the instrument was quite stable,

with a σ(RV) of 1.5 m s^{-1} or better. On other nights, however, we see much greater variability, with σ(RV) of approximately 10 m s^{-1} and peak-to-peak fluctuations as large as 20 m s^{-1}. The "unstable" nights seem to be due to temperature fluctuations of ~ 0.2 °C of the optomechanical structure of the instrument, induced by ~ 5 °C changes of the ambient air temperature in the room housing the dFTS2 hardware. Even though the air temperature inside the dFTS2 enclosure is controlled to ± 0.05 °C, the optical breadboard and optics mounts can get warmer or cooler and change their shape enough to induce a measurable RV shift. To account for this error source, we apply an error of 10 m s^{-1} (added in quadrature) to the RV error estimates for all our stellar observations, as well as adjusting the RV zero point on a night-by-night basis (see below). Future dFTS instruments will need to be installed in more thermally stable environments to achieve their full RV measurement potential.

## 5. DATA REDUCTION AND DERIVATION OF RADIAL VELOCITIES

Reduction of the interferogram data from dFTS2 followed the same basic pathway as for dFTS1 (see Section 3.4 of Paper 1), with the addition of an intermediate step to correct for a significant nonlinearity in the response of the U-1107 CCD. Photometric corrections were particularly important for these data, as seeing fluctuations and passing thin clouds would often change the stellar flux by a factor of 2 or 3 from one exposure to the next. By using the unfringed "C-track," which was picked off from the main starlight beam before it entered the interferometer, we were able to normalize the flux levels over the course of a scan, so that only true interferometric fringes remained.

To determine a topocentric RV for each observation, we compared the normalized interferograms to synthetic interferograms derived from a Doppler-shifted template spectrum. We sampled the synthetic interferograms at the same delays as each observation scan, and we scanned through a range of RVs until we found a smooth global minimum in the χ^2 difference between the data and the model. This technique incorporated the optimal weighting of the data and provided an estimate of the internal statistical error in RV for each observation.

We employed two different types of template spectra for these RV fits. For the first template, we used the FROID algorithm, described in detail in Paper 1, to turn the parallel
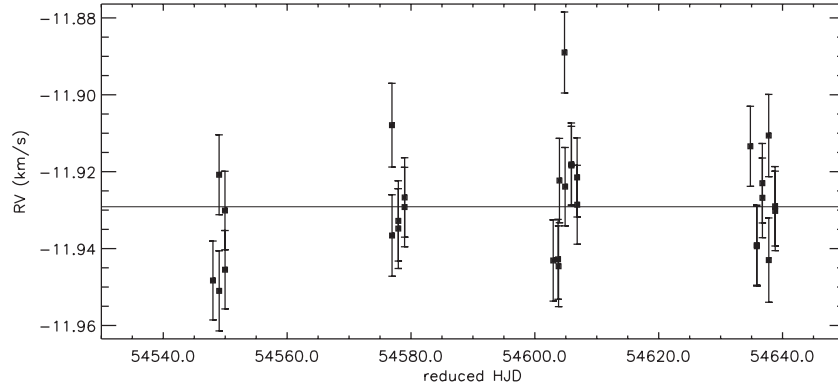
Figure 6. Radial velocity measurements of the K2III star β Ophiuchi, with an rms scatter of 13.6 m s^{-1}.
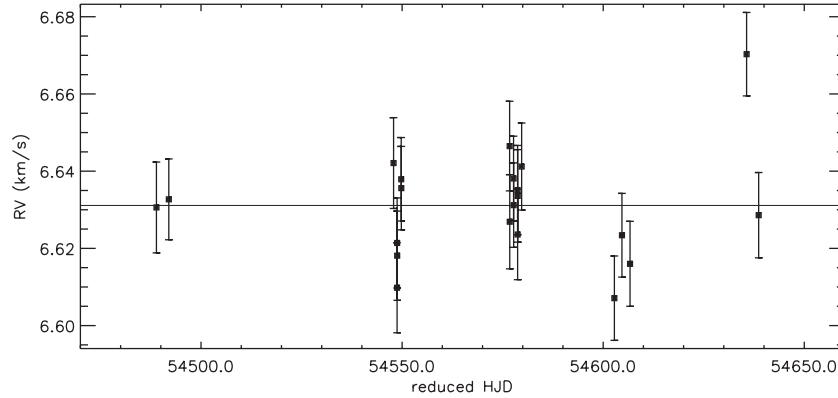
Figure 7. Radial velocity measurements of the G0V star β Canum Venaticorum, with an rms scatter of 13.8 m s^{-1}.

narrowband interferograms into a single high-resolution ($R =$ 50,000) broadband spectrum for each observation. All derived spectra for a given star were then shifted to zero Doppler velocity and co-added to make a template specific to that star. The second template type was generated using the SPECTRUM spectral synthesis package (Gray & Corbally 1994; see also http://www.phys.appstate.edu/spectrum/spectrum.html) and ATLAS9 model atmosphere grids (Kurucz 1993). We found that spectra generated using the default atomic line list resulted in sub-optimal RV solutions, because the depths of the synthetic absorption lines were not perfectly matched to the actual spectra. By adjusting the transition strength log gf of each line individually (sometimes increasing, sometimes decreasing), we were able to create synthetic templates which performed as well as the co-added templates. All of the RV results presented below were derived using synthetic spectral templates instead of co-added templates, but the RV results were very similar in all cases.

As a final step, we converted the topocentric velocities into barycentric velocities using the IRAF tool BCVCORR. We also applied an additional velocity correction factor based on the mean thorium–neon velocity offset for each night of observing, to account for RV shifts due to instrument realignment. We did not make any adjustment for the varying light travel time within the binary systems, since the resulting change in RV is small compared to the RV measurement errors.

6. RV MEASUREMENTS OF REFERENCE STARS

To verify that dFTS2 was stable, we observed three astronomical targets which were expected to maintain a constant barycentric RV over time.

6.1. β Ophiuchi

The star β Ophiuchi (HR 6603, HD 161096, HIP 86742) is a K2III giant with an apparent V magnitude of 2.77 and no known binary companion. We made 30 observations of β Oph between 2008 March and June, and the heliocentric RV data are plotted in Figure 6. The RV points exhibit an rms scatter of 13.6 m s^{-1} around the mean. The RV error is dominated by the temperature-induced instrument instability mentioned in Section 4.3. Without this source of systematic error, we estimate that we could have achieved a mean RV accuracy of 2.1 m s^{-1} per observation on β Oph, based upon χ^2 analysis of photon statistics in the interferogram data.

6.2. β Canum Venaticorum

The G0V star β Canum Venaticorum (HR 4785, HD 109358, HIP 61317) was our second RV reference star. At $V = 4.26$, it tested the RV performance of our instrument at lower flux levels. Figure 7 depicts our RV results. We find an rms scatter of the barycentric RV points of 13.8 m s^{-1}, similar to that of β Oph because the error budget is dominated by the same systematic error sources. If we were limited solely by photon statistics and CCD read noise, we estimate that dFTS2 could achieve a per-observation RV accuracy of 5.1 m s^{-1} on this star.

6.3. The Moon

As our third RV test target, we observed sunlight reflected from the bright lunar crater Mösting A, which provided a flux level similar to a $V = 2.8$ star. We used lunar ephemerides calculated with the MICA package (Oliversen et al. 2005) to shift the measured velocities to a common reference frame. The
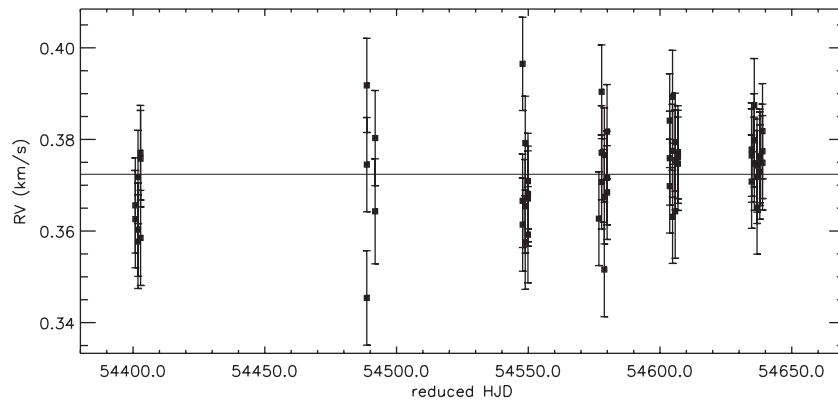
Figure 8. Radial velocity measurements of the G2V solar spectrum reflected from the lunar crater Mösting A. The rms scatter of the velocity points is 9.7 m s^{-1}.
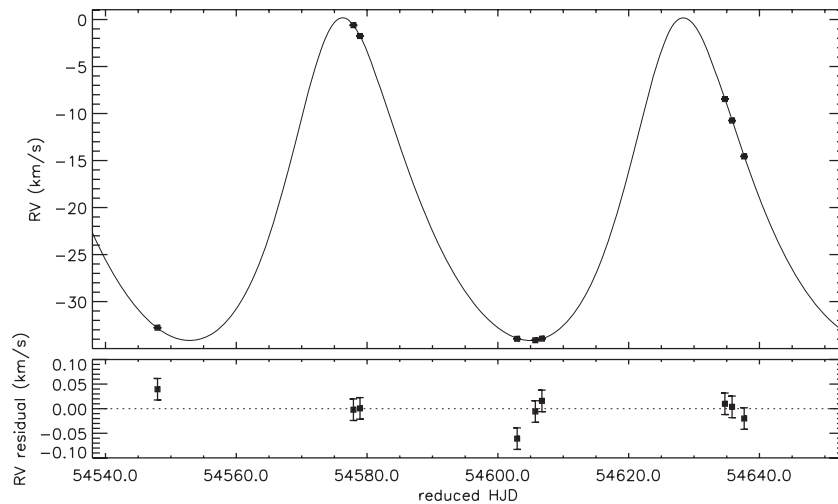
Figure 9. Radial velocity measurements of the F6V star 19 Draconis. The rms scatter of the velocity residuals is 27.5 m s^{-1}.

resulting time series of velocities, shown in Figure 8, has an rms scatter of 9.7 m s^{-1}. The mean internal error bar from photon statistics is 2.5 m s^{-1} for these observations.

7. RV MEASUREMENTS OF SB1 TARGETS

During our time at the Bok Telescope, we observed a variety of single-lined (SB1) and double-lined (SB2) spectroscopic binary systems. The results for the SB1s are described below, while the orbital fits for the SB2s will be reported in a following publication. We had hoped to collect ~40 RV points for each binary, well distributed over the orbital phase, in order to derive the binary parameters with higher accuracy than ever before. Unfortunately, bureaucratic considerations led to the decommissioning of the dFTS2 instrument in 2008 August, and thus the end of our observing program. As a result, none of our orbital RV curves are well sampled, and for systems with $P > 100$ days we do not even cover a full orbit. The orbital parameters that we derive from our RV measurements should therefore be considered as preliminary results, which serve primarily to illustrate the potential usefulness of dFTS instrumentation for the accurate determination of binary star orbits.

For deriving orbital parameters from our RV data, we used the IDL routines CURVEFIT, a nonlinear least-squares fitting algorithm included with the IDL package, and HELIO_RV, which computes binary star orbit velocities (Landsman 1993). In all cases, we adopted the orbital period P from previously published

analyses, because we had too few data points to derive an accurate value.

7.1. 19 Draconis

The 19 Draconis system (HR 6315, HD 153597, HIP 82860) consists of a F6V star with $V = 4.89$ co-orbiting with an unseen companion. With only nine RV observations, we could not constrain the orbital period, so we adopted $P = 52.1089$ days from Abt & Levy (1976) but let all other orbital parameters vary in the fitting algorithm. Figure 9 shows the RV points and the resulting orbit, with parameters $T_{\rm peri} = 54\,522.258 \pm 0.121$ days, $V_0 = -20.5299 \pm 0.0649$ km s^{-1}, $K = 17.1590 \pm 0.0344$ km s^{-1}, $e = 0.2218 \pm 0.0020$, and $\omega = 339°.1 \pm 0°.6$. The uncertainty on the value of K yields a fractional uncertainty $\Delta K/K$ of 0.20%.

The RV residuals show an rms scatter of 27.5 m s^{-1}, while the mean formal error bar was 21.3 m s^{-1}, with $\chi^2 = 12.19$ for $\nu = 4$. We used the formal error bars in calculating the parameter uncertainties cited above. If these error bars are scaled such that the mean error bar is equal to the rms scatter, then the uncertainty on K increases to 0.0444 km s^{-1}, or $\Delta K/K = 0.26\%$. With relatively few data points, it is difficult to tell whether this discrepancy between the formal RV errors and the RV residual rms is just a statistical aberration, or is indicative of an additional RV error source, such as stellar pulsation or the spectral contribution of the faint secondary. As pointed out by our anonymous referee, contamination from the
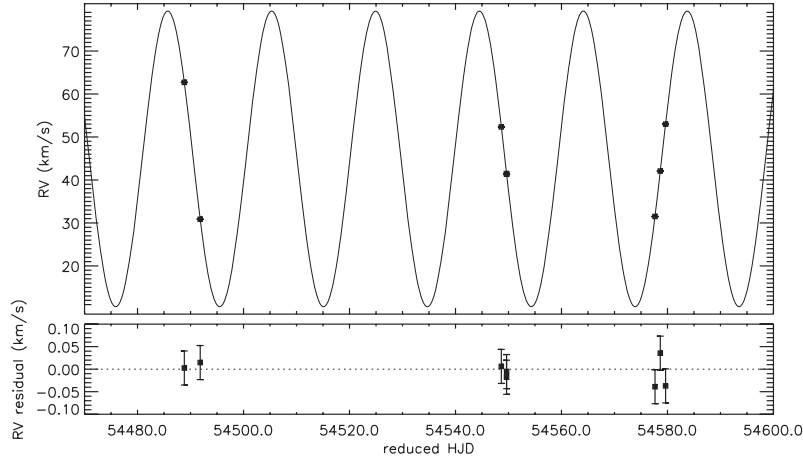
Figure 10. Radial velocity measurements of the K1III star σ Geminorum. The rms scatter of the velocity residuals is 25.5 m s^{-1}.
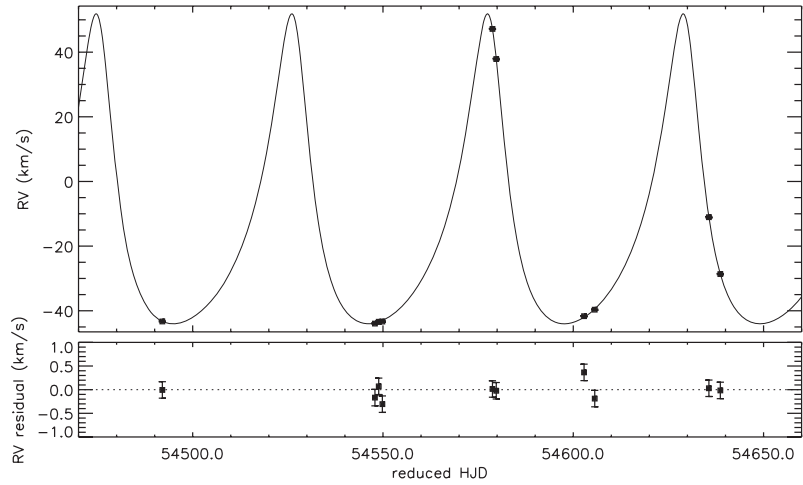
Figure 11. Radial velocity measurements of the A0III star α Draconis. The rms scatter of the velocity residuals is 180.3 m s^{-1}.

secondary spectrum can add noise to RV measurements of the primary. Using the Hipparcos parallax (Perryman et al. 1997) for 19 Dra, we calculate an absolute magnitude of $M_V = 4.00$, or $L_1 \simeq 2.15\,L_\odot$, assuming that the primary dominates the total system flux. Based on the F6V spectral type, we estimate $M_1 \simeq 1.26\,M_\odot$. Using the mass function for the system and $i = 56°1$ from Jancart et al. (2005), we can then estimate $M_2 \simeq 0.54\,M_\odot$, or $L_2 \simeq 0.12\,L_\odot$ for a main-sequence star. The secondary might therefore account for 6% of the total flux in V band, which could be enough to influence the measured velocities for the primary, and might also be detectable. Future analysis work will attempt to detect the secondary spectrum, or place more stringent limits on its brightness.

7.2. σ Geminorum

The star σ Geminorum (HR 2973, HD 62044, HIP 37629) has a V magnitude of 4.28 and a spectral type of K1III. It is also listed as a RS CVn variable, and our measurements of spectral line widths imply a projected rotation velocity of 23.5 km s^{-1}, which may be related to its chromospheric activity level. Our RV measurements and best-fit orbit are plotted in Figure 10. As with 19 Dra, we adopt $P = 19.6044$ days from the literature (Massarotti et al. 2008) and then derive: $T_{\rm peri} = 54\,603.597 \pm 0.189$ days, $V_0 = 44.4206 \pm 0.0502$ km s^{-1}, $K = 34.3931 \pm 0.0456$ km s^{-1}, $e = 0.0141 \pm 0.0017$, and $\omega = 5°1 \pm 3°5$. The rms scatter of the RV residuals is 25.5 m s^{-1},

as compared to a mean formal RV error bar of 29.8 m s^{-1}, and $\chi^2 = 4.50$ for $\nu = 3$. The formal uncertainty on K implies $\Delta K / K = 0.11\%$, but because none of our RV points are located near velocity maxima or minima, this K value should be considered tentative at best and does not supersede the Massarotti results.

Using a similar procedure as with 19 Dra, we estimate a luminosity of $23\,L_\odot$ for the σ Gem system. The spectral type of K1III implies a mass $M_1 = 4.2\,M_\odot$ for the primary. The orbital inclination angle of this binary is unknown, but assuming $\sin i = 90°$, we find a minimum mass $M_2 = 1.6\,M_\odot$, which for a main-sequence star implies $L_2 = 5.6\,L_\odot$, and thus $L_1 = 17.4\,L_\odot$. The secondary is therefore at least one third of the brightness of the primary, and should be visible in the composite spectrum. However, our data are not suitable for attempting this detection, as all of our measured primary velocities are near the systemic velocity, where the primary's spectral lines are likely to overlap heavily with those of the secondary.

7.3. α Draconis

α Draconis (HR 5291, HD 123299, HIP 68756) is an A0III star with $V = 3.65$ and an estimated $v \sin i = 26.6$ km s^{-1}. Adopting $P = 51.4167$ days (Elst & Nelles 1983), we find our RV data (Figure 11) are best fit by an orbit with $T_{\rm peri} = 54\,527.112 \pm 0.075$ days, $V_0 = -15.5899 \pm 0.3035$ km s^{-1},
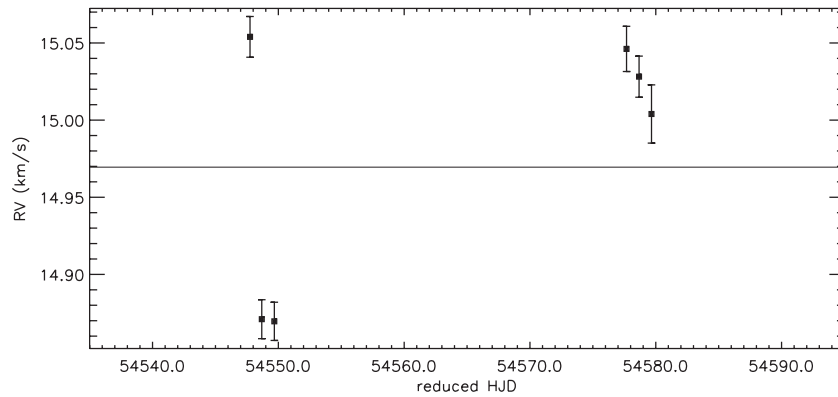
Figure 12. Radial velocity measurements of the F6IV star θ Ursae Majoris.

Table 1
The SB1 Orbital Parameters Derived from dFTS2 Observations

Star	P (days)	$T_{\rm peri}$ (reduced JD)	V_0 (km s^{-1})	K (km s^{-1})	e	ω (°)
19 Dra	52.1089	54522.258 ± 0.121	-20.5299 ± 0.0649	17.1590 ± 0.0344	0.2218 ± 0.0020	339.1 ± 0.6
σ Gem	19.6044	54603.597 ± 0.189	44.4206 ± 0.0502	34.3931 ± 0.0456	0.0141 ± 0.0017	5.1 ± 3.5
α Dra	51.4167	54527.112 ± 0.075	-15.5899 ± 0.3035	47.9340 ± 0.2990	0.4355 ± 0.0042	20.8 ± 0.5

$K = 47.9340 \pm 0.2990$ km s^{-1}, $e = 0.4355 \pm 0.0042$, and $\omega = 20°.8 \pm 0°.5$. Our determination of $\Delta K/K$ is thus 0.62%. The mean formal error bar (172.9 m s^{-1}) and the rms of the RV residuals (180.3 m s^{-1}) are larger than the other targets because hot stars have so few strong metal lines in their optical spectra. The orbital fit gives $\chi^2 = 9.61$ with $\nu = 5$.

From the apparent magnitude and Hipparcos parallax of this system, we estimate $L \simeq 270\,L_\odot$. Because A0III is a rare spectral type (perhaps in a transitional state between two types of chemically peculiar A stars; Adelman et al. 1987), it is challenging to determine an appropriate mass. Kallinger et al. (2004) claimed $M_1 = 2.8\,M_\odot$, which we will adopt. Using our mass function and assuming $i = 90°$, we find $M_2 \simeq 2.6\,M_\odot$, which corresponds to a A2V spectral type with $L \simeq 40\,L_\odot$. The secondary could therefore account for 15% of the total luminosity of this system.

7.4. θ Ursae Majoris

θ Ursae Majoris (HR 3775, HD 82328, HIP 46853, F6IV, $V = 3.20$) is listed in SIMBAD as a spectroscopic binary, but it does not appear in the SB9 binary catalog, and Wittenmyer et al. (2006) found no evidence of RV periodicity above ~ 20 m s^{-1}. We made six observations of this star during two different observing runs. We find that its RV changed by about 180 m s^{-1} peak to peak, although our data do not fit any obvious Keplerian orbit (Figure 12). We hope to make further RV measurements of this star during future observing programs, to more firmly establish its binary status.

8. SUMMARY

We have described the design and operation of dFTS2, a next-generation incarnation of the dFTS concept. This spectrometer produces $R = 50,000$ stellar optical spectra, with a wavelength calibration that enables accurate RV measurement. The photon throughput and grating resolution of dFTS2 are significantly improved over its predecessor, resulting in better spectral accuracy on fainter stars, but thermal drifts inside the instrument limit its RV stability to ~ 10 m s^{-1}. Given a stable instrument temperature, our thorium–neon calibration data indicate that

dFTS2 can reach RV stability better than 1.5 m s^{-1} rms. These temperature issues will be addressed in a future dFTS instrument, at which point the RV accuracy will be limited primarily by photon statistics and intrinsic stellar velocity variability.

We have shown that dFTS2 can accurately measure the RV curves of single-lined spectroscopic binaries, with formal errors on the velocity amplitude K of approximately 0.1% in some cases. Table 1 summarizes the derived orbital parameters. However, some of our results must be considered preliminary because of the relatively small number of data points. When the third-generation dFTS has been constructed and deployed, we anticipate being able to significantly improve the RV measurements of spectroscopic binaries, and in conjunction with astrometry from spatial interferometers, determine the masses of stars with unprecedented accuracy.

REFERENCES

Abt, H. A., & Levy, S. G. 1976, ApJS, 30, 273
Adelman, S. J., Bolcal, C., Kocer, D., & Inelmen, E. 1987, PASP, 99, 130
Bouchy, F., et al. 2009, A&A, 496, 527
Elst, E. W., & Nelles, B. 1983, A&AS, 53, 215
Fekel, F. C., Williamson, M., & Pourbaix, D. 2007, AJ, 133, 2431
Gray, R. O., & Corbally, C. J. 1994, AJ, 107, 742
Hajian, A. R., et al. 2007, ApJ, 661, 616
Hearnshaw, J. B., Barnes, S. I., Kershaw, G. M., Frost, N., Graham, G., Ritchie, R., & Nankivell, G. R. 2002, Exp. Astron., 13, 59
Howard, A. W., et al. 2009, ApJ, 696, 75
Jancart, S., Jorissen, A., Babusiaux, C., & Pourbaix, D. 2005, A&A, 442, 365
Kallinger, T., Iliev, I., Lehmann, H., & Weiss, W. W. 2004, in IAU Symp. 224, The A-Star Puzzle, ed. J. Zverko, J. Ziznovsky, S. J. Adelman, & W. W. Weiss (Cambridge: Cambridge Univ. Press), 848
Konacki, M. 2005, ApJ, 626, 431
Konacki, M. 2009, in IAU Symp. 253, Transiting Planets, ed. F. Pont, D. Sasselov, & M. Holman (Cambridge: Cambridge Univ. Press), 141
Kurucz, R. 1993, ATLAS9 Stellar Atmosphere Programs and 2 km/s grid, Kurucz CD-ROM No. 13 (Cambridge, MA: Smithsonian Astrophysical Observatory), http://kurucz.harvard.edu/
Landsman, W. B. 1993, in ASP Conf. Ser. 52, Astronomical Data Analysis Software and Systems. II., ed. R. J. Hanisch, R. J. V. Brissenden, & Jeannette Barnes (San Francisco, CA: ASP), 246
Massarotti, A., Latham, D. W., Stefanik, R. P., & Fogel, J. 2008, AJ, 135, 209
McCarthy, J. K., Sandiford, B. A., Boyd, D., & Booth, J. 1993, PASP, 105, 881
Muterspaugh, M. W., Lane, B. F., Konacki, M., Wiktorowicz, S., Burke, B. F., Colavita, M. M., Kulkarni, S. R., & Shao, M. 2006, ApJ, 636, 1020
Oliversen, N. A., Harris, W. T., Puatua, W. K., Tangren, W. J., Bangert, J. A., Kaplan, G. H., & Janiczek, P. M. 2005, BAAS, 37, 1217
Perryman, M. A. C., et al. 1997, A&A, 323, L49
Pourbaix, D., et al. 2004, A&A, 424, 727
Ramm, D. J. 2008, MNRAS, 387, 220
Ramm, D. J., Skuljan, J., & Hearnshaw, J. B. 2004, Observatory, 124, 167
Skuljan, J., Ramm, D. J., & Hearnshaw, J. B. 2004, MNRAS, 352, 975
Tomkin, J., & Fekel, F. C. 2006, AJ, 131, 2652
Wittenmyer, R. A., Endl, M., Cochran, W. D., Hatzes, A. P., Walker, G. A. H., Yang, S. L. S., & Paulson, D. B. 2006, AJ, 132, 177